# A compact aqueous K-ion Micro-battery by a Self-shrinkage assembly strategy

Yuyang Han [a],[1], Chunlong Dai [a],[1], Jingguo Lin [b], Feng Liu [b], Hongwei Ma [c], Ying Wang [a], Bing Lu [a], Changxiang Shao [a], Qiang Guo [a], Xuting Jin [a], Xinqun Zhang [a], Zhipan Zhang [a],[*]

[a] Key Laboratory of Cluster Science, Ministry of Education, Beijing Key Laboratory of Photoelectronic/Electrophotonic Conversion Materials, School of Chemistry and Chemical Engineering, Beijing Institute of Technology, Beijing 100081, PR China
[b] State Key Laboratory of Nonlinear Mechanics, Institute of Mechanics Chinese Academy of Sciences, Beijing 100190, PR China
[c] Analysis and Testing Center, Beijing Institute of Technology, Beijing 100081, PR China

## ARTICLE INFO

## ABSTRACT

Micro-batteries are promising power sources to drive miniaturized or portable electronic devices due to their higher energy density than micro-supercapacitors. Current micro-batteries still suffer from relatively large footprint and unsatisfactory areal electrochemical performance caused by loose electrode structure. Here, we develop a compact aqueous K-ion micro-battery through the self-shrinking of reduced graphene oxide hydrogel to realize small footprint and high areal capacity at the same time. With a volume of as small as $0.00381 \text{ cm}^{-3}$, this micro-battery delivers the highest areal capacity ($5.1 \text{ mAh cm}^{-2}$) and energy density ($4.78 \text{ mWh cm}^{-2}$) among all reported micro-batteries. Meanwhile, this micro-battery can be prepared into different shapes and attached onto a range of animals (ants, crabs and butterflies, etc.) for wide applications.

## 1. Introduction

With the fast development of portable and wearable electronics, it is urgent to explore compatible miniaturized power sources to drive these electronic devices [1,2]. Although micro-supercapacitors show advantages of fast charge/discharge rates and long service life, they suffer from some intrinsic drawbacks including self-discharge and low energy density. Compared to micro-supercapacitors, micro-batteries feature slower self-discharge, higher capacity and energy density for long-term operation of micro-devices.

Currently, micro-batteries are mainly prepared with in-plane interdigital structures that lead to a series of problems. First, interdigitally-patterned micro-batteries generally employ excessive current collectors [3–5] and substrates [5–7], resulting in a relatively large footprint (approximately *ca.* 2 cm$^2$). In addition, since the electrode easily delaminates from the current collector under a high active material loading, it is difficult to achieve high areal capacity. For example, Zheng et.al reported a rechargeable Na-ion micro-battery with an excellent volumetric capacity of $30.7 \text{ mAh cm}^{-3}$, but its areal capacity was limited to $0.08 \text{ mAh cm}^{-2}$ as the thickness of the electrodes cannot exceed 25 μm

[8]. Lai et. al reported a $Zn//MnO_2$ micro-battery with a high volume capacity of $28.3 \text{ mAh cm}^{-3}$, yet its areal capacity was only $0.55 \text{ mAh cm}^{-2}$ as the result of the low active material loading [4]. To solve this issue, a three-dimensional sandwiched structure was proposed to achieve high active material loading and the highest areal capacity of $2.5 \text{ mAh cm}^{-2}$ [9]. Unfortunately, electrodes of these micro-batteries were mainly prepared by electrodeposition [10–12] and slurry-coating methods [9] and typically have a loose electrode structure, thus resulting in mainly point contact between the small particles inside the electrode, which further leads to slow ion/electron conduct and high internal resistance. Moreover, these micro-batteries are short of the accuracy control for the microelectrodes material to face complicated power systems demand and suffer from the high weight, which limit immensely their multi-scenario application. Thus, it is challenging to develop high-areal-capacity micro-batteries that can be applied in a wide range of scenarios.

Herein, we have adopted a self-shrinkage assembly strategy to fabricate a compact aqueous K-ion micro-battery (CKMB) with a light weight (5 mg), small footprint ($0.0156 \text{ cm}^{-2}$), and high areal capacity ($5.1 \text{ mAh cm}^{-2}$). Reduced graphene oxide (rGO) hydrogel was found to

---
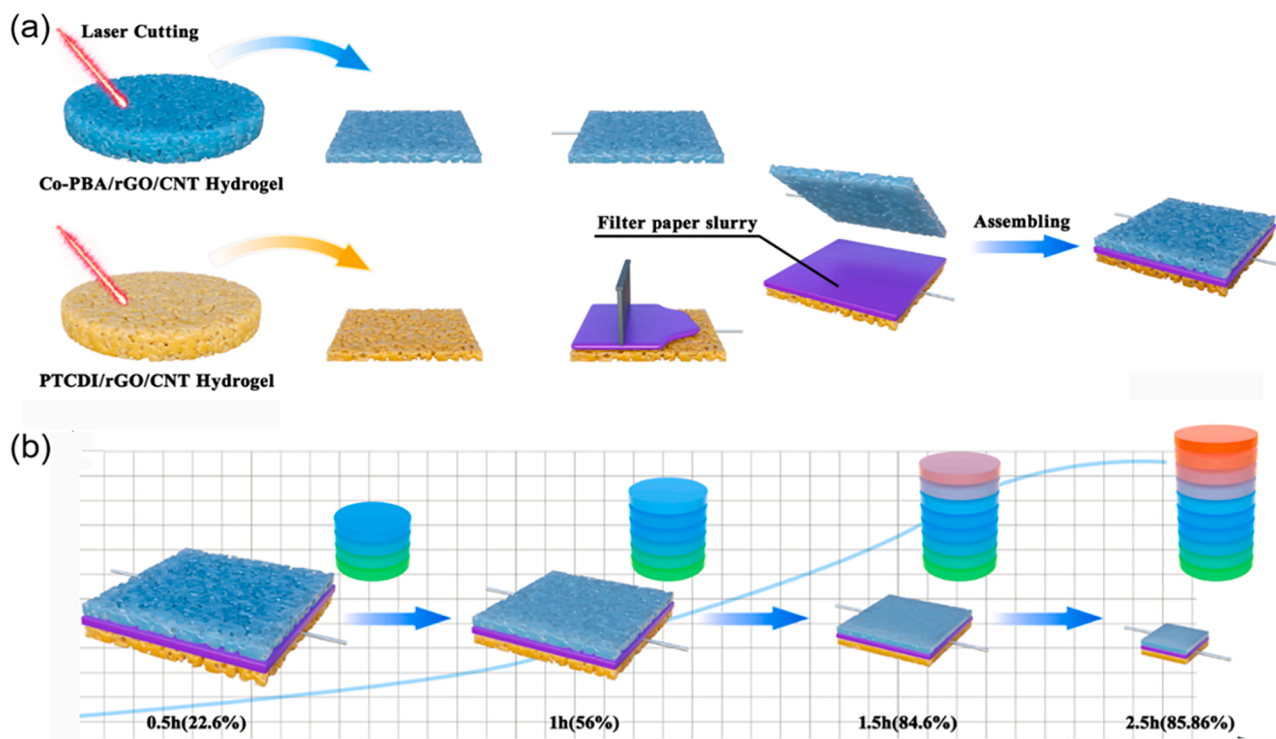
**Scheme 1.** The fabrication and characterization of the CKMB. Schematic illustration of (a) preparation process and (b) the shrinkage assembly process of CKMB. The related volume shrink ratios are 22.6%, 56%, 84.6%, and 85.9% at shrinking time of 0.5, 1, 1.5, 2, and 2.5 h, respectively. The colorful cylindrical piece symbols the energy bar.

shrink spontaneously into a compact and dense structure at ambient conditions with the evaporation of water [13], rendering a new avenue to prepare thick and made-to-measure micro-electrodes with high loadings of active materials. Due to the abundance and favorable intercalation/extraction reaction kinetics of K ions [14–18], the rechargeable K-ion micro-batteries are selected to demonstrate this concept. In addition, benefiting from the operable laser processing and excellent plasticity of the hydrogel electrode material, the CKMB can be easily attached to a range of animals to supply power in aerial (on butterflies), aquatic (on crabs) and terrestrial (on ants) scenarios.

## 2. Materials and methods

### 2.1. Materials

cobalt nitrate hexahydrate, sodium citrate, potassium ferricyanide, carbon nanotube (CNT) and 3,4,9,10-perylenetetracarboxylic diimide (PTCDI) were purchased from Aladdin Industries. All chemicals were of analytical grade and used as received.

### 2.2. Preparation of Co-PBA (Cobalt Prussian blue analogue)

0.3 M cobalt nitrate hexahydrate and 0.45 M sodium citrate Dispersed in deionized (DI) water, known as solution A. Solution B contains 0.2 M potassium ferricyanide and DI water. Mix solution A and B and stir them to form uniform solution. After quiescence at room temperature for about 14 days, the Co-PBA was prepared. The collected samples were washed with DI water and ethanol for several times, and then dried at 70 °C for 12 h.

### 2.3. Preparation of Prussian blue (PB)

First, 0.3 M ferrous chloride and 0.45 M sodium citrate were

dispersed in deionized (DI) water and the solution is mixed with 0.2 M potassium ferricyanide solution. The mixture was left in air at room temperature for about 14 days before the collected PB sample was washed by DI water and ethanol for several times and then dried at 70 °C for 12 h.

### 2.4. Preparation of cathode material

Graphene oxide (GO) was prepared with 2 mg mL$^{-1}$ according to the modified Hummers method. Mix the Co-PBA, GO (2 mg mL$^{-1}$) and CNT in a mass ratio of 200, 60, 15 under stirring for 4 h to form uniform solution, and then add into a Teflon-lined autoclave. In order to acquire the homogeneous cathode hydrogel, the solution in Teflon-lined autoclave was treated by 95 °C for 3 h and then 180 °C for 3 h, forming a cylindrical Co-PBA/rGO/CNT hydrogel.

### 2.5. Preparation of anode material

Mix the PTCDI, GO (2 mg mL$^{-1}$) and CNT in a mass ratio of 200, 60, 30, and then referr to the above preparation step of cathode material, forming a cylindrical PTDCL/rGO/CNT hydrogel.

### 2.6. Laser engraving the electrode material

The graphene hydrogel with the cylindrical shape was first cut into wafer-shape with the centimeter-level thickness by a 355 nm ultraviolet laser cutting system (Beijing Lagamin Laser Co., LM-UVY-5S-Y). The frequency was set as 30 kHz, with a scan speed of 100 mm s$^{-1}$, current as 1 A and a pulse width as 10 μs. Then, the hydrogel wafer could be further processed into different pre-designed shapes with the aid of Ezcad2 software, such as of circle, star, heart and alphabetic letters. A frequency of 80 kHz, a scan speed of 80 mm s$^{-1}$, current as 1 A, and a pulse width of 5 μs were used in this process.
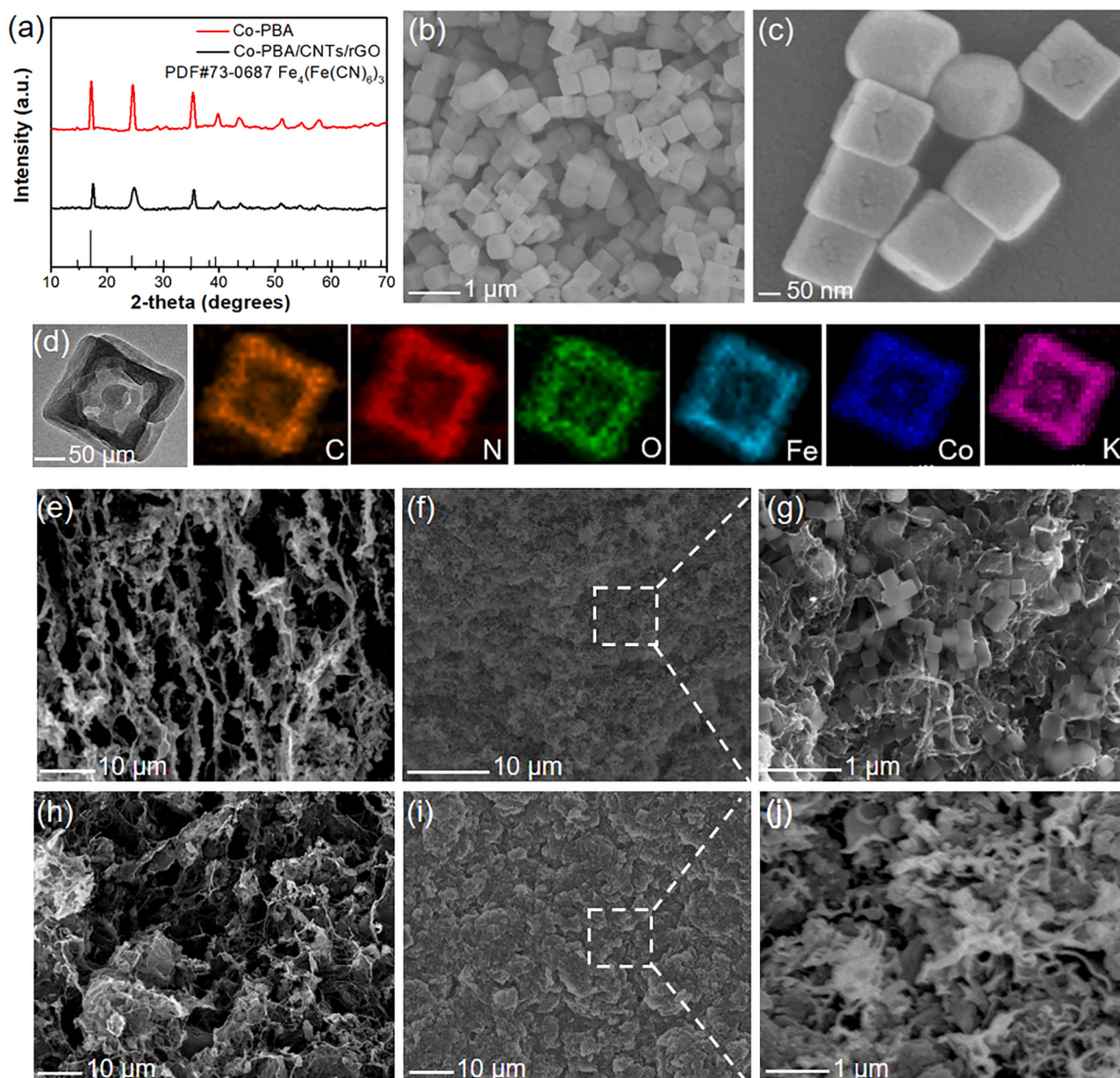
**Fig. 1.** The characterizations of the electrode materials. (a) XRD pattern of the pure Co-PBA and as-prepared Co-PBA/CNTs/rGO. The (b and c) SEM, (d) TEM images, and elemental mappings of the pure Co-PBA sample. The SEM images of Co-PBA/CNTs/rGO cathode (e) before shrinking and (f and g) after shrinking. The SEM images of PTCDI/CNTs/rGO anode (h) before shrinking and (i and j) after shrinking.

## 2.7. Preparation of separator

Mix the filter paper with the gelatin solution, smashed with the high speed blender, resulting in a homogeneous liquid slurry.

## 2.8. Characterization and measurements

The morphology of the prepared materials were characterized using Scanning electron microscope (SEM, JSM-7001F) and Transmission electron microscopy (TEM, FEI TECNAI TF20, USA). The Energy dispersive spectroscopy (EDS) data was examined by JEOL-6300F. X-ray diffraction (XRD) were conducted by Rigaku MiniFlex 600 diffractometer with Cu-Kα X-ray radiation to confirm the crystal structures. The laser cutting was conducted by ultraviolet laser (Beijing Lagamin Laser Co., LM-UVY-5S-Y).

The cyclic voltammetry (CV) measurements were performed by the

CHI760 workstation at ambient condition (Shanghai Chenhua, China) with scan rates from 0.3 to 1 mV s$^{-1}$. The remaining electrochemical measurements were conducted on the Land cycler (Wuhan Kingnuo Electronic Co., China). The galvanostatic charge–discharge (GCD) behaviors were performed by the Land cycler (Wuhan Kingnuo Electronic Co., China). The area specific capacity and energy density were calculated based on the opposite area between the cathode and anode. The area specific capacity and energy density were calculated based on the opposite area between the cathode and anode. The volume specific capacity were calculated based on the whole volume for the battery. The gravimetric specific capacity were calculated based on the mass of active material.

## 3. Results and discussion

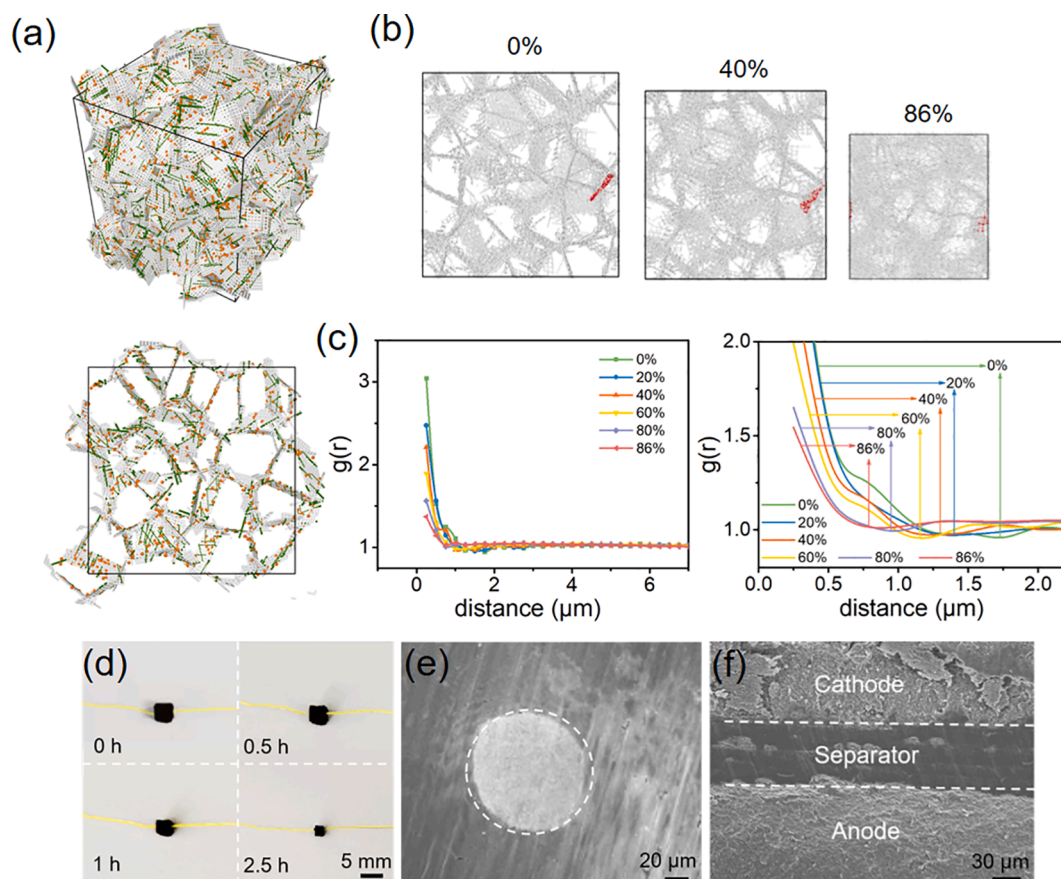Scheme 1a depicts the fabrication of the CKMB *via* the self-shrinkage

**Fig. 2.** Shrinkage simulation of the CKMB. (a) The coarse grain molecular dynamics model Co-PBA/CNTs/rGO, where white particles sheets represent rGO, green particles chains represent CNTs, and orange particles are used to indicate Co-PBA particles. To facilitate observe the internal porous structure, one slice of the model is given at the bottom. (b) Microstructure evolution of Co-PBA/CNTs/rGO with volume reducing by 0%, 40% and 86%. (c) The obtained radial distribution function is shown, with part of it zoom in on the right. Note that the dots are statistical results of 5 samples and are fitted with Bezier curves. The short-range correlation (the region with distance less than 0.7 μm) and the characteristic correlation valleys are marked with the corresponding colored lines for different contraction degrees. (d) The photograph of the shrinkage assembly process for the practical CKMB. (e) Cross-section SEM image of the implanted Au current collector in the electrode. (f) Cross-section SEM image of the prepared CKMB with the sandwich structure.

assembly strategy. Briefly, Co-PBA and PTCDI were selected as active materials in the cathode and anode, respectively and separately added in a GO/CNT mixed solution to prepare the Co-PBA/rGO/CNT or PTCDI/rGO/CNT hydrogel through a temperature-change hydrothermal reduction process that favored a homogeneous structure for the Co-PBA/rGO/CNT hydrogel and PTCDI/rGO/CNT hydrogel [13]. Here, Co-PBA and PTCDI were chosen due to their long-term stability against water [19–22], where CNT was used to improve the conductivity of the electrode and rGO acted as the shrinking matrix, respectively. The two hydrogels were then laminated with the filter paper slurry as the separator to form the aqueous CKMB. Driven by the capillary force during the water evaporation process, the CKMB shrank gradually to 0.00381 cm$^{-3}$, which was one-seventh of its original volume (Scheme 1b), leaving the device with a compact structure and improved areal capacity.

Fig. 1a shows the XRD patterns of the bare Co-PBA and Co-PBA/CNTs/rGO cathode [20–22]. Furthermore, the XRD pattern of as-prepared Co-PBA/CNTs/rGO cathode are similar with the pure Co-PBA, demonstrating Co-PBA could withstand the high temperate in the hydrothermal process and maintains the original structure, In addition, the broadening peaks at 2-theata of 24.8° in the XRD pattern demonstrates a decrease in crystallinity after combining the CNTs and rGO material [23]. As shown in Fig. 1b and 1c, Co-PBA features a nanocube shape with an average size of about 200 nm and the small size facilitating its even dispersion in the GO/CNT

solution to form a homogeneous composite. In addition, Fig. 1d displays the elemental mappings of the pure Co-PBA, confirming the unique square hollow framework structure and homogeneous distribution of the elements (Fig. S1). Such a square hollow framework structure would allow a strong interaction with the electrolyte for an improved specific capacity and fast charge/discharge rates in the CKMB [24]. The morphology of the Co-PBA/CNTs/rGO cathode during the self-shrinkage was characterized by SEM. As shown in Fig. 1e, the original foam-like structure in the as-prepared Co-PBA/CNTs/rGO cathode gradually disappears and appears the compact structure, where the surface tension induces the aggregation of rGO flakes during the water evaporation and leads to the substantially shrank to 6 times smaller than the original Co-PBA/CNTs/ rGO after 2.5 h. The magnifed SEM image in Fig. 1g, the Co-PBA with the cubic structure and CNTs with the rod structure disperses homogeneous on the rGO flakes. As for the anode material, PTCDI particles feature an irregular rectangular shape that can be confirmed by the SEM image (Fig S2a). In addition, the XRD pattern of the PTCDI is shown to be similar to previous PTCDI derivatives [25]. As shown in Fig. S2b, the primary peaks at 2-*theta* of 12.1°, 19.8°, 24.8°, 30.4° can be ascribed to diffractions between (021), (002), (11_2), (12_2), and (140) planes of monoclinic PTCDI crystals (space group: P21/n), respectively. Naturally, the PTCDI/rGO/CNT anode features a similar morphological change during the self-shrinkage process (Fig. 1f-1j and Fig. S3).
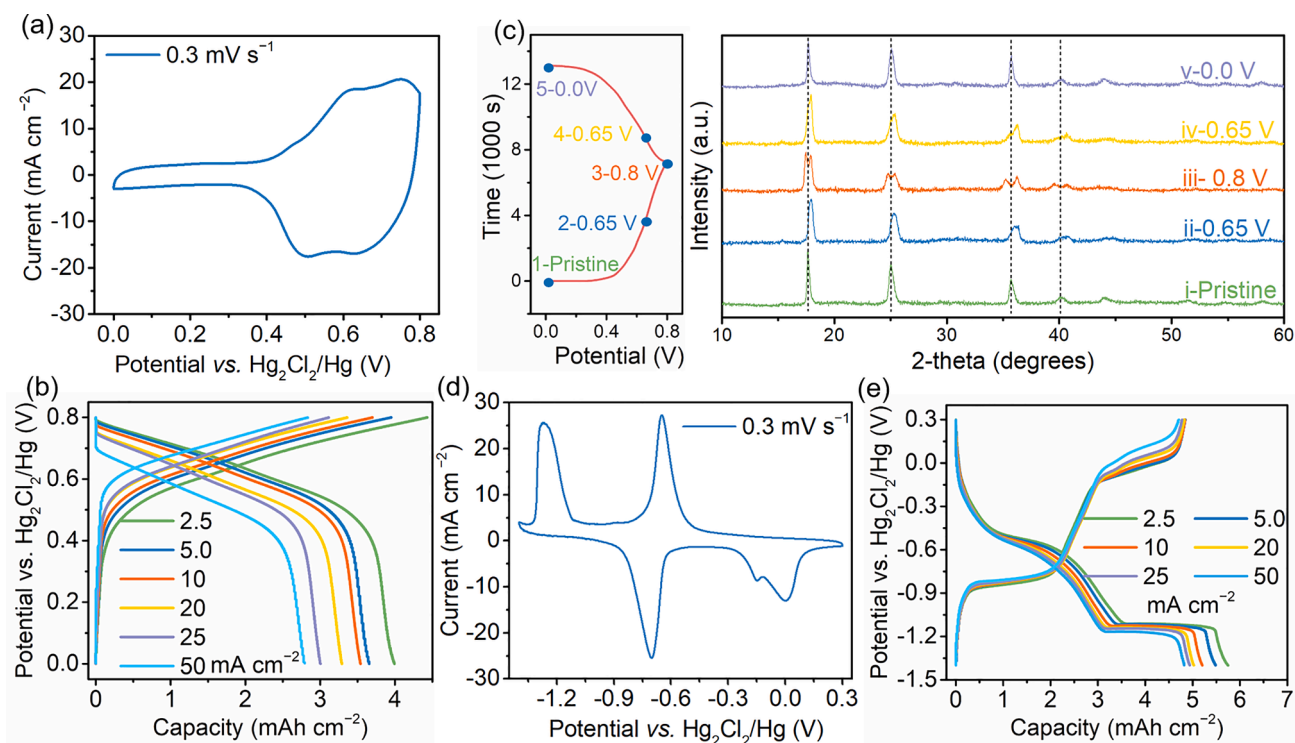
**Fig. 3.** The electrochemical performance of the compact cathode and anode based on the three-electrode system. (a) The representative CV curves and (b) GCD profiles of compact Co-PBA/CNTs/rGO cathode. (c) The GCD curve of Co-PBA at 30 mA g$^{-1}$ and corresponding structural evolution at appointed potential depicted by XRD patterns. (d) The representative CV curves and (e) GCD curves of compact PTCDI/CNTs/rGO anode.

One of the concerns is whether the porous microstructure features is uniformly stressed and maintained during the contraction process. To address this issue, a coarse grain molecular dynamics simulation is employed. As shown in Fig. 2a, the Co-PBA/CNTs/rGO configuration is generated *via* Voronoi tessellation to reflect the porous microstructure, where the structural skeleton is composed by rGO sheets with embedded CNTs and Co-PBA nanoparticles. In our coarse grain model, a graphene sheet is represented by a 7 × 7 coarse grain particles connected by harmonic interaction, a CNT is approximately considered as a chain and made up by 12 coarse grain particles, and a Co-PBA nanoparticle is just described by one coarse grain particle. The contraction process is simulated by uniformly and continuously reducing the simulation box size (details could be found in supplementary information). The corresponding microstructure evolution is given in Fig. 2b. To facilitate visualizing the structural skeleton evolution, only rGO sheets are shown in this plot. It could be seen that a well-established porous microstructure at the beginning gradually blurs due to rGO sheets deviation (mainly rotation and bending) from their initial Voronoi face, which is consistent with experimental observed structural densification. In Fig. 2b, rGO sheets within a given Voronoi face are tracked (marked with red color), and an obvious deviation from the Voronoi face could be seen and eventually a folding occurs. In fact, the microscopic mechanism of the densification origins from the random arrangement of rGO sheets, instead of a group bending deformation they tend to bend individually due to their different neighbor configurations. A quantitative analysis is given in Fig. 2c, where the radial distribution function (RDF) of the mean coordinates of rGO sheets in one Voronoi face at the beginning is measured, and the local part of RDF is zoomed in. Five samples are used to obtain RDF, and there is a short-range correlation appears before 0.8 μm (much less than the rGO sheet size of 3 μm and the Voronoi face size of ～ 6 μm), representing the Voronoi intra-face rGO sheets correlation. A clear tendency is that with the self-contraction process, the short-range correlation decreases, manifesting the above-mentioned deviation of

rGO sheets from their initial Voronoi face and thus suppresses the Voronoi intra-face rGO sheets correlation. Besides, the characteristic correlation valleys are marked with the corresponding colored vertical lines for RDF curves at different contraction degrees. As the system contracts uniformly, the position of the characteristic correlation valleys evenly varies to a shorter distance, suggesting that the porous microstructure nearly takes homogenous deformation in the entire process (Fig. 2d). Therefore, the original microstructure of rGO is still reversed to a certain extent, and no new microstructure features are found except for a structural densification that is induced by part of the graphene sheets deviating from its relative position. In addition, the densification structure also enables a firm connection between the electrodes and the separator or Au current collector as shown in Fig. 2e and 2f. It is worth noting that this self-shrinkage process is at the device level, avoiding electrode patterning, slurry preparation and coating in the fabrication of conventional micro-batteries, thus improving the device integration and adaptability for multi-scenario applications.

The electrochemical performance of the compact cathode and anode was first tested in a three-electrode system with a carbon counter electrode, a saturated calomel reference electrode, and an electrolyte of 22 M KCF$_3$SO$_3$. Fig. 3a presents the typical CV curves of the Co-PBA/CNTs/rGO cathode at a scan rate of 0.3 mV s$^{-1}$ between 0 and 0.8 V. The reduction peaks are at about 0.65 and 0.5 V and the oxidation peaks are at about 0.6 and 0.75 V. The reduction peaks represent the processes of K$^+$ ions intercalation into Co-PBA, and the oxidation peaks mean the removal of K$^+$ ions from Co-PBA [26]. Fig. 3b shows the corresponding GCD behaviors of the PBA/CNTs/rGO cathode at different current densities, the main discharge range is at about 0.8 to 0.4 V, and delivers a high capacity of 5.1 mAh cm$^{-2}$ at 2.5 mA cm$^{-2}$ (49.6 mAh g$^{-1}$). The pure Co-PBA cathode shows a gravimetric specific capacity of 57.7 mAh g$^{-1}$, which is considerably higher than that of the control device based on Prussian blue (PB) cathode (20.74 mAh g$^{-1}$, Fig. S4 and S5). The structural evolution of the cathode
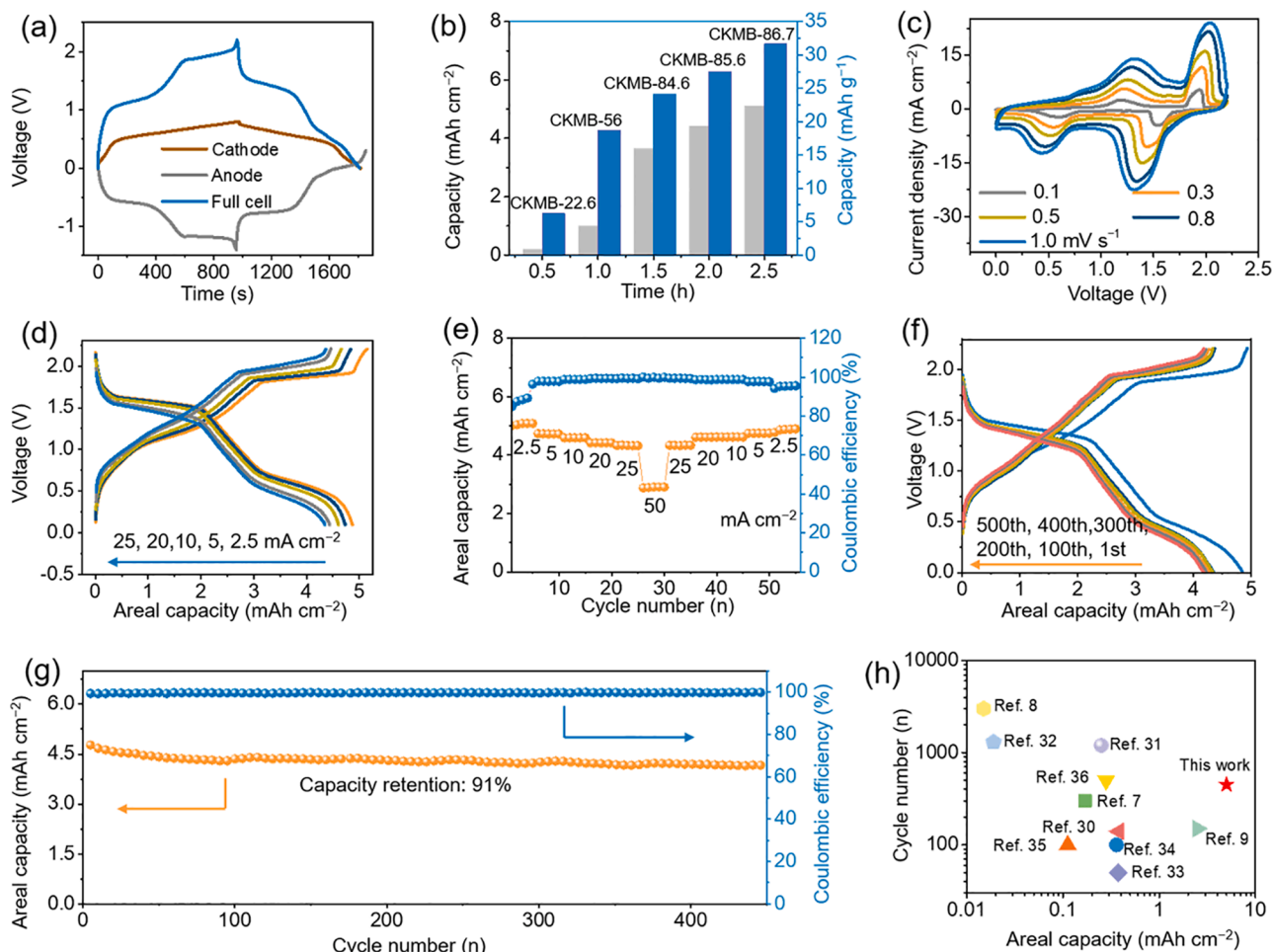
**Fig. 4.** Electrochemical performances of the aqueous CKMB. (a) The pairing curves of the full CKMB. (b) The comparisons of capacity under different shrinking degree. The typical (c) CV curves, (d) GCD curves, and (e) rate performance of the CKMB. (f-g) The cycling stability of the full CKMB at 25 mA cm$^{-2}$ current densities. (h) The comparison of this CKMB with recent reported micro-batteries.

during the electrochemical process was analyzed by the ex-situ XRD characterizations. As shown in Fig. 3c, the Co-PBA cathode is poised at different potentials and its XRD pattern is measured. During the charging process, the peaks at 2-*theta* of 17.5°, 24.8°, 35.4° and 39.8° gradually shift rightward to 17.9°, 25.3°, 36.1° and 40.5°, respectively, suggesting the decreased lattice size of the Co–PBA due to the extraction of K$^+$. Upon the discharging process, these peaks shift back to the initial position due to the K$^+$ insertion [27,28] and this pattern remains unchanged even after cycling for 450 times (Fig. S6), highlighting its reversible electrochemistry. Fig. 3d shows the CV curve of the PTCDI/ CNTs/rGO anode at 0.3 mV s$^{-1}$ between − 1.4 and 0.3 V. It shows two pairs of redox peaks, which is consistent with the previous report [29]. Fig. 3e exhibits the corresponding GCD curves of the anode at various current densities. There are two main discharging plateaus at about − 0.5 and − 1.2 V, respectively, and two main charging plateaus at about − 0.8 and 0.1 V, respectively. The GCD curve of the PTCDI/CNTs/rGO anode at 50 mA cm$^{-2}$ is similar to that at 2.5 mA cm$^{-2}$, suggesting the excellent rate performance of the anode. High capacities of 160 mAh g$^{-1}$ and 5.1 mAh cm$^{-2}$ are achieved for the anode even at high current density of 1.6 A g$^{-1}$ and 50 mA cm$^{-2}$, further demonstrating the excellent rate capability (Fig. S5c).

The cathode and the anode are then paired to make a full CKMB (Fig. 4a). To better elucidate the influence of the self-shrinking process on the performance of the battery, its electrochemical performance was studied at different shrinkage time. The contraction percentage of the

CKMB was 22.6%, 56%, 84.6%, 85.6%, 85.7% at 0.5, 1, 1.5, 2, and 2.5 h, respectively (Fig. 2d). As shown in Fig. 4b, both the gravimetric and areal specific capacity of the CKMB gradually get better with the shrinkage, confirming the effectiveness of this self-shrinkage assembly strategy. Electrochemical impedance spectroscopy results in Fig. S7 demonstrate that the charge-transfer resistance between the electrode–electrolyte interface that is determined from the semicircle in the high-frequency region of the Nyquist plot decreased drastically with the shrinkage, indicating the contraction process is beneficial to expedite the charge transfer kinetics. As displayed in Fig. 4c, CV curves of the CKMB at various scan rates from 0.1 to 1 mV s$^{-1}$ retain the essential shape, demonstrating the exceptional rate capability. As shown in Fig. 4d, the potential plateau in the GCD curves of the CKMB is in accordance with the CV features, whose behaviors can be described as the K ions migration from the anode to the cathode at the discharging process and migration reversely at the charging process. At the meanwhile, Fig. 4d exhibits the excellent rate capability under different current densities, delivering reversible discharge capacities of 4.3, 4.4, 4.6, 4.7, and 5.0 mAh cm$^{-2}$ (20 mAh cm$^{-3}$) under current densities of 25, 20, 10, 5, 2.5 mA cm$^{-2}$ (10 mA cm$^{-3}$) (Fig. S8), in which the mass loading of cathode and anode are ca. 1.9 mg and 0.5 mg, respectively. As shown in Fig. 4e, even though the CKMB suffer high current density of 50 mA cm$^{-2}$, the remarkable capacity can be recovered when the current densities set back, further confirming the excellent rate stability of the CKMB. Fig. 4f displays the 1st, 100 th, 200 th, 300 th, 400 th and 450
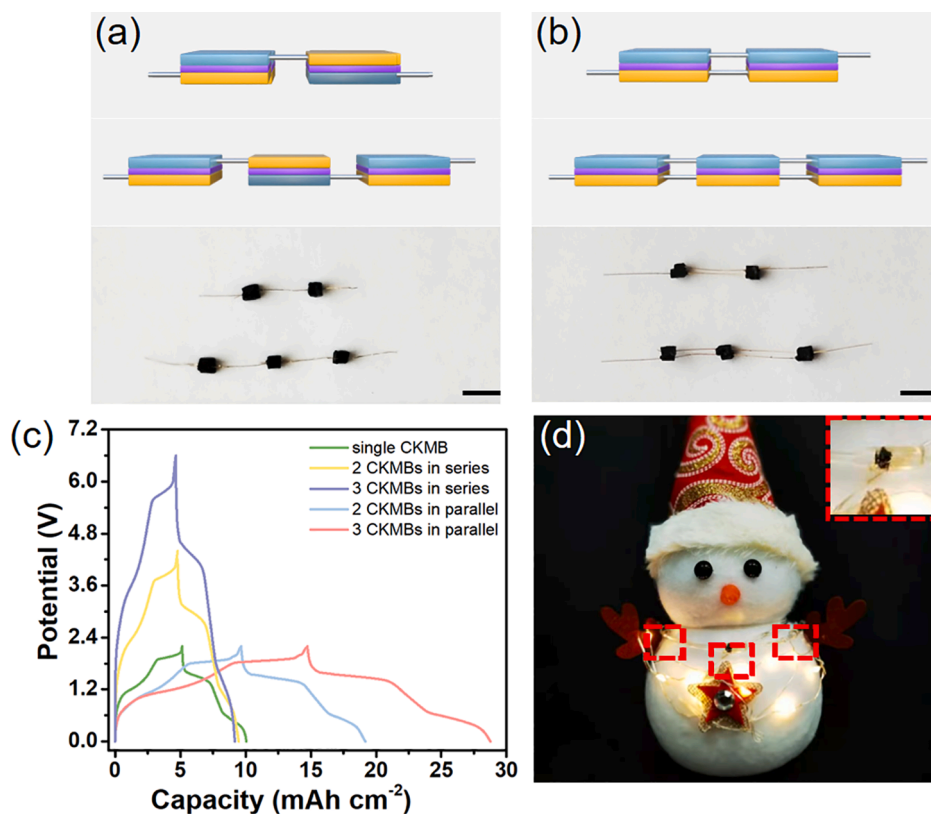
**Fig. 5.** Schematic illustration and electrochemical performance of CKMB with series or parallel connection. The schematic diagram of the CKMB (a) in series and (b) in parallel. (c) The electrochemical performance of a single CKMB, two CKMBs, and three CKMBs in series or parallel connection. (d) A photograph of the 10 commercial LEDs lighted by the three CKMBs in series connection. The CKMB is signed in the dashed box and the scale bar is 2 mm.

th GCD curves of CKMB at 25 mA cm$^{-2}$, in which the primary plateaus and capacity basically maintain, indicating the CKMB can operate stably between the potential window from 0 V to 2.2 V. Finally, the full battery CKMB delivers an extraordinary cycling stability, with 91% capacity retention and coulombic efficiency of 99.9% over 450 cycles at 25 mA cm$^{-2}$ (Fig. 4g). XRD patterns for the electrode materials after 450 cycles show that the peak position well matched the pristine materials (Fig. S6), implying the excellent stability of CKMB. When compared with other reported micro-batteries (lithium ion micro-batteries, sodium ion micro-batteries, zinc ion micro-batteries, and dual ion micro-batteries) [7–9,30–36], the CKMB shows the highest areal capacity with a decent cycling lifetime (Fig. 4h).

Due to the compact structure of the CKMB, it can be connected in series or parallel to achieve higher voltage and current output. For instance, two and three CKMBs can be easily connected in series or parallel with the Au current collector (Fig. 5a and 5b), respectively. As shown in Fig. 5c, two and three series-connected CKMBs can deliver a voltage of 4.4 V and 6.6 V, respectively, which well corresponds to the double and triple voltage of a single CKMB. Moreover, the CKMBs with parallel connection can deliver higher capacity proportionally as our expectation, indicating the CKMBs are able to adapt the electronic devices with the high energy demand by series or parallel connection. As exhibited in Fig. 5d, a necklace composed of three CKMBs connected in-series can light 10 LEDs for more than 30 min (Movie S1).

The strategy to prepare the CKMB by shrinking at the device level enables the fabrication of micro-batteries with pre-designed complicated geometries. As displayed in Fig. 6a, CKMBs with shapes of circle, star, heart and alphabetic letters can be easily prepared. Besides the programmable function, light-weight feature of the CKMB (the whole device is only 5 mg) makes it possible to work on small animals.

For instance, a circular CKMB can be designed and attached to an ant's body without interference on its normal behavior (Fig. 6b). The CKMB can also be attached onto a butterfly for lighting up an LED, providing opportunities to track its positions even in the dark (Fig. 6c). More impressively, the aqueous nature of the CKMB enables it to work underwater with the unchanged electrochemical performance as shown in Fig. S9. When placed the CKMB on a crab, it could adequately power an LED in water (Fig. 6d and Movie S2), qualifying it as a new type of light-weighted power device that operates in all terrestrial situations.

## 4. Conclusion

In conclusion, a CKMB has been constructed through a self-shrinkage assembly strategy. Driven by the capillary force during the water evaporation process, the CKMB shrinks to one-seventh of its original volume, realizing a compact structure, which is beneficial to fast electron transfer. Besides, the self-shrinkage assembly strategy endows CKMB with light weight (5 mg), small footprint (0.0156 cm$^{-2}$), and high areal capacity (5.1 mAh cm$^{-2}$). Benefiting from its light weight, outstanding electrochemical performance, and excellent plasticity, the CKMB could be attached to a range of animals to supply power, such as on butterflies, crabs, and even ants without significantly affecting their activities, demonstrating its potential applications in aerial, aquatic, and terrestrial scenarios.

## Declaration of Competing Interest

The authors declare that they have no known competing financial interests or personal relationships that could have appeared to influence the work reported in this paper.
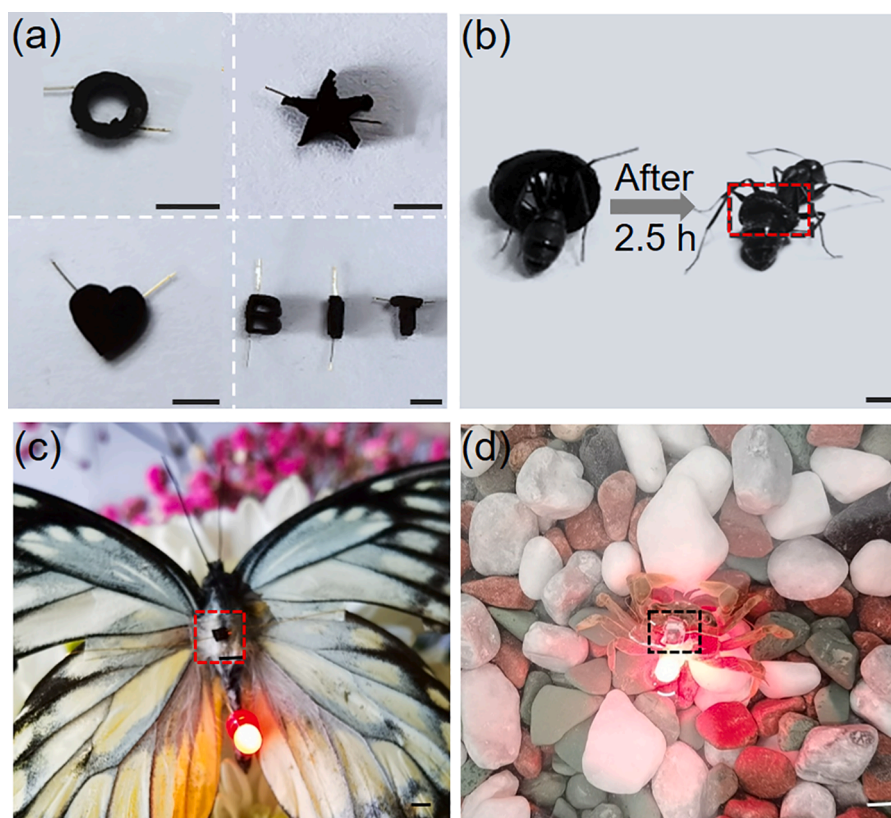
**Fig. 6.** The multi-functions exhibition for CKMB. (a) Shape-programmability of CKMB for various situations. (b) The special design of CKMB with concentric circles shape for ant. (c) The CKMB designed as electronic power on butterflies. (d) The CKMB applied on crabs. The CKMB is signed in the dashed box and the scale bar is 2 mm.

## Acknowledgements

## Appendix A. Supplementary data

Supplementary data to this article can be found online at https://doi.org/10.1016/j.cej.2021.132291.

## References

[1] Y. Wang, Y. Zhao, L. Qu, Laser fabrication of functional micro-supercapacitors, J. Energy Chem. 59 (2021) 642–665, https://doi.org/10.1016/j.jechem.2020.12.002.

[2] Y. Liu, Z. Sun, X. Sun, Y. Lin, K.e. Tan, J. Sun, L. Liang, L. Hou, C. Yuan, Construction of hierarchical nanotubes assembled from ultrathin V₃S₄@C nanosheets towards alkali-ion batteries with ion-dependent electrochemical mechanisms, Angew. Chem. Int. Ed. 59 (6) (2020) 2473–2482, https://doi.org/10.1002/anie.v59.610.1002/anie.201913343.

[3] Y.Q. Li, H. Shi, S.B. Wang, Y.T. Zhou, Z. Wen, X.Y. Lang, Q. Jiang, Dual-phase nanostructuring of layered metal oxides for high-performance aqueous rechargeable potassium ion microbatteries, Nat. Commun. 10 (1) (2019) 4292, https://doi.org/10.1038/s41467-019-12274-7.

[4] W. Lai, Y. Wang, Z. Lei, R. Wang, Z. Lin, C.P. Wong, F. Kang, C. Yang, High performance, environmentally benign and integratable Zn//MnO₂ microbatteries, J. Mater. Chem. A 6 (9) (2018) 3933–3940, https://doi.org/10.1039/C7TA10936A.

[5] S. Zheng, Z.S. Wu, F. Zhou, X. Wang, J. Ma, C. Liu, Y.B. He, X. Bao, All-solid-state planar integrated lithium ion micro-batteries with extraordinary flexibility and high-temperature performance, Nano Energy 51 (2018) 613–620, https://doi.org/10.1016/j.nanoen.2018.07.009.

[6] G. Sun, X. Jin, H. Yang, J. Gao, L. Qu, An aqueous Zn–MnO₂ rechargeable microbattery, J. Mater. Chem. A 6 (23) (2018) 10926–10931, https://doi.org/10.1039/C8TA02747A.

[7] Q. Liu, G. Zhang, N. Chen, X. Feng, C. Wang, J. Wang, X. Jin, L. Qu, The first flexible dual-ion microbattery demonstrates superior capacity and ultrahigh energy density: small and powerful, Adv. Funct. Mater. 30 (38) (2020) 2002086, https://doi.org/10.1002/adfm.v30.3810.1002/adfm.202002086.

[8] S. Zheng, H. Huang, Y. Dong, S. Wang, F. Zhou, J. Qin, C. Sun, Y. Yu, Z.S. Wu, X. Bao, Ionogel-based sodium ion micro-batteries with a 3D Na-ion diffusion mechanism enable ultrahigh rate capability, Energy Environ. Sci. 13 (3) (2020) 821–829, https://doi.org/10.1039/C9EE03219C.

[9] M. Nasreldin, R. Delattre, C. Calmes, M. Ramuz, V.A. Sugiawati, S. Maria, J.-L. Tocnaye, T. Djenizian, High performance stretchable Li-ion microbattery, Energy Storage Mater. 33 (2020) 108–115, https://doi.org/10.1016/j.ensm.2020.07.005.

[10] G.F. Ortiz, M.C. López, R. Alcántara, J.L. Tirado, Electrodeposition of copper–tin nanowires on Ti foils for rechargeable lithium micro-batteries with high energy density, J. Alloy. Compd. 585 (2014) 331–336, https://doi.org/10.1016/j.jallcom.2013.09.163.

[11] G. Oltean, M. Valvo, L. Nyholm, K. Edström, On the electrophoretic and sol–gel deposition of active materials on aluminium rod current collectors for three-dimensional Li-ion micro-batteries, Thin Solid Films 562 (2014) 63–69, https://doi.org/10.1016/j.tsf.2014.03.069.

[12] Z. Jin, P. Li, Y. Jin, D. Xiao, Superficial-defect engineered nickel/iron oxide nanocrystals enable high-efficient flexible fiber battery, Energy Storage Mater. 13 (2018) 160–167, https://doi.org/10.1016/j.ensm.2018.01.010.

[13] B. Lu, F. Liu, G. Sun, J. Gao, T. Xu, Y. Xiao, C. Shao, X. Jin, H. Yang, Y. Zhao, Z. Zhang, L. Jiang, L. Qu, Compact assembly and programmable integration of supercapacitors, Adv. Mater. 32 (6) (2020) 1907005, https://doi.org/10.1002/adma.v32.610.1002/adma.201907005.

[14] H. Kim, J. Hong, K.Y. Park, H. Kim, S.W. Kim, K. Kang, Aqueous rechargeable Li and Na ion batteries, Chem. Rev. 114 (23) (2014) 11788–11827, https://doi.org/10.1021/cr500232y.

[15] E.R. Nightingale, Phenomenological Theory of Ion Solvation. Effective radii of hydrated ions, J. Phys. Chem 63 (9) (1959) 1381–1387.

[16] A. Esfandiar, B. Radha, F.C. Wang, Q. Yang, S. Hu, S. Garaj, R.R. Nair, A.K. Geim, K. Gopinadhan, Size effect in ion transport through angstrom-scale slits, Science 358 (6362) (2017) 511–513, https://doi.org/10.1126/science:aan5275.

[17] Z. Sun, Y. Liu, W. Ye, J. Zhang, Y. Wang, Y. Lin, L. Hou, M.-S. Wang, C. Yuan, Unveiling intrinsic potassium storage behaviors of hierarchical nano Bi@N-doped carbon nanocages framework via in situ characterizations, Angew. Chem. Int. Ed. 60 (13) (2021) 7180–7187, https://doi.org/10.1002/anie.v60.1310.1002/anie.202016082.

[18] G. Qin, Y. Liu, F. Liu, X. Sun, L. Hou, B. Liu, C. Yuan, Magnetic field assisted construction of hollow red p nanospheres confined in hierarchical N-doped carbon nanosheets/nanotubes 3D framework for efficient potassium storage, Adv. Energy Mater. 11 (4) (2021) 2003429, https://doi.org/10.1002/aenm.v11.410.1002/aenm.202003429.

[19] J. Qian, C. Wu, Y. Cao, Z. Ma, Y. Huang, X. Ai, H. Yang, Prussian blue cathode materials for sodium-ion batteries and other ion batteries, Adv. Energy Mater. 8 (17) (2018) 1702619, https://doi.org/10.1002/aenm.v8.1710.1002/aenm.201702619.

[20] C.D. Wessells, S.V. Peddada, R.A. Huggins, Y. Cui, Nickel hexacyanoferrate nanoparticle electrodes for aqueous sodium and potassium ion batteries, Nano Lett. 11 (12) (2011) 5421–5425, https://doi.org/10.1021/nl203193q.

[21] C.D. Wessells, R.A. Huggins, Y. Cui, Copper hexacyanoferrate battery electrodes with long cycle life and high power, Nat. Commun. 2 (1) (2011) 550, https://doi.org/10.1038/ncomms1563.

[22] D. Su, A. McDonagh, S.-Z. Qiao, G. Wang, High-capacity aqueous potassium-ion batteries for large-scale energy storage, Adv. Mater. 29 (1) (2017) 1604007, https://doi.org/10.1002/adma.v29.110.1002/adma.201604007.

[23] Y. Sun, C. Liu, J. Xie, D. Zhuang, W. Zheng, X. Zhao, Potassium manganese hexacyanoferrate/graphene as a high-performance cathode for potassium-ion batteries, New J. Chem. 43 (29) (2019) 11618–11625, https://doi.org/10.1039/C9NJ02085C.

[24] J. Jiang, G. Nie, P. Nie, Z. Li, Z. Pan, Z. Kou, H. Dou, X. Zhang, J. Wang, Nanohollow carbon for rechargeable batteries: ongoing progresses and challenges, Nano-Micro Lett. 12 (1) (2020) 183, https://doi.org/10.1007/s40820-020-00521-2.

[25] W. Deng, Y. Shen, J. Qian, Y. Cao, H. Yang, A perylene diimide crystal with high capacity and stable cyclability for Na-ion batteries, ACS Appl. Mater. Interfaces 7 (38) (2015) 21095-21099, https:10.1021/acsami.5b04325.

[26] X. Wu, S. Qiu, X. Yu, Y.u. Ma, X. Bi, Y. Yuan, T. Wu, R. Shahbazian-Yassar, J. Lu, X. Ji, Hydrous nickel–iron turnbull's blue as a high-rate and low-temperature proton electrode, ACS Appl. Mater. Interfaces 12 (8) (2020) 9201–9208, https://doi.org/10.1021/acsami.9b2032010.1021/acsami.9b20320.s001.

[27] Y. You, X.L. Wu, Y.X. Yin, Y.G. Guo, A zero-strain insertion cathode material of nickel ferricyanide for sodium-ion batteries, J. Mater. Chem. A 1 (45) (2013) 14061–14065, https://doi.org/10.1039/C3TA13223D.

[28] X. Bie, K. Kubota, T. Hosaka, K. Chihara, S. Komaba, A novel K-ion battery: hexacyanoferrate(ii)/graphite cell, J. Mater. Chem. A 5 (9) (2017) 4325–4330, https://doi.org/10.1039/C7TA00220C.

[29] Y. Bai, W. Fu, W. Chen, Z. Chen, X. Pan, X. Lv, J. Wu, X. Pan, Perylenetetracarboxylic diimide as a high-rate anode for potassium-ion batteries, J. Mater. Chem. A 7 (42) (2019) 24454–24461, https://doi.org/10.1039/C9TA07605K.

[30] C. Yue, Y. Yu, J. Yin, T. Wong, Y. Zang, J. Li, J. Kang, Fabrication of 3D hexagonal bottle-like Si–SnO$_2$ core–shell nanorod arrays as anode material in on chip micro-lithium-ion-batteries, J. Mater. Chem. A 1 (27) (2013) 7896–7904, https://doi.org/10.1039/C3TA10601B.

[31] G.D. Salian, B.M. Koo, C. Lefevre, T. Cottineau, C. Lebouin, A.T. Tesfaye, P. Knauth, V. Keller, T. Djenizian, Niobium alloying of self-organized TiO$_2$ nanotubes as an anode for Lithium-ion microbatteries, Adv. Mater. Technol. 3 (3) (2018) 1700274, https://doi.org/10.1002/admt.v3.310.1002/admt.201700274.

[32] V.A. Sugiawati, F. Vacandio, N. Yitzhack, Y. Ein-Eli, T. Djenizian, Direct pre-lithiation of electropolymerized carbon nanotubes for enhanced cycling performance of flexible Li-ion micro-batteries, Polymers 12 (2) (2020) 406, https://doi.org/10.3390/polym12020406.

[33] M. Hallot, A. Demortière, P. Roussel, C. Lethien, Sputtered LiMn$_{1.5}$Ni$_{0.5}$O$_4$ thin films for Li-ion micro-batteries with high energy and rate capabilities, Energy Storage Mater. 15 (2018) 396–406, https://doi.org/10.1016/j.ensm.2018.08.012.

[34] A.T. Tesfaye, O. Mashtalir, M. Naguib, M.W. Barsoum, Y. Gogotsi, T. Djenizian, Anodized Ti$_3$SiC$_2$ as an anode material for Li-ion microbatteries, ACS Appl. Mater. Interfaces 8 (26) (2016) 16670–16676, https://doi.org/10.1021/acsami.6b0352810.1021/acsami.6b03528.s001.

[35] R. Li, L.a. Li, R. Jia, K. Jiang, G. Shen, D.i. Chen, A flexible concentric circle structured Zinc-ion micro-battery with electrodeposited electrodes, Small Methods 4 (9) (2020) 2000363, https://doi.org/10.1002/smtd.v4.910.1002/smtd.202000363.

[36] X. Wang, S. Zheng, F. Zhou, J. Qin, X. Shi, S. Wang, C. Sun, X. Bao, Z.S. Wu, Scalable fabrication of printed Zn//MnO$_2$ planar micro-batteries with high volumetric energy density and exceptional safety, Natl. Sci. Rev. 7 (1) (2019) 64–72, https://doi.org/10.1093/nsr/nwz0.